

Supporting Information for

**Final-State Simulations of Core-Level Binding Energies at
Metal-Organic Hybrid Interfaces: Artifacts Caused by
Spurious Collective Electrostatic Effects**

Thomas C. Taucher, Oliver T. Hofmann, and Egbert Zojer*

Institute of Solid State Physics, Graz University of Technology, NAWI Graz, Petersgasse 16, 8010 Graz,
Austria.

*Corresponding author: egbert.zojer@tugraz.at

Table of Content

1. Dependence of the core-level binding energies on molecular coverage.....	3
2. Methodological details and tests	5
2.1. Information on the employed basis functions.....	5
2.2. Convergence of the k-point grid.....	6
2.3. Impact of the number of layers contained in the slab	7
2.4. Impact of the geometric relaxation of the topmost metal layer	8
2.5. Spin polarized calculations	8
3. Charge rearrangements due to the excitation.....	10
3.1. Plane-integrated charge rearrangements	11
3.2. Plane integrated rearrangements as a function of the adsorption distance.....	12
3.3. Cumulative charge rearrangements as a function of the adsorption distance ...	13
4. Shift of electronic levels	15
4.1. Work function shifts	15
4.2. Electrostatic model for estimating work-function changes	16
4.3. Carbon 1s core-level binding energies	16
5. Half core-hole vs. full core-hole calculations	17
6. Final-state calculations relying on the Δ SCF approach.....	18
7. Impact of the core-hole excitations on the work function on the Al-side of the slab	20
8. Impact of locality effects of the electrostatic energy on core-level binding energies	21
8.1. Dependence of evolution of the local electrostatic energy on the size over which the lateral averaging occurs	23
9. Fermi-level pinning for large adsorption heights and small unit cells	25
10. HOMO – LUMO gap	31
11. Electrical field for a CREST-type compensation charge	32
12. References.....	34

1. Dependence of the core-level binding energies on molecular coverage

In the main manuscript we show that the C 1s core-level binding energies of methane adsorbed on a Al(100) surface calculated employing the final-statefinal-state approach strongly depends on the density of core holes present in the simulation. These results (shown in Figure 2a of the main manuscript) have been obtained when modeling the binding energies as a function of supercell size with one excitation per supercell. In these simulations, the coverage of the methane molecules was kept constant. In Figure S1 we show that essentially the same results are obtained when also varying the coverage of the methane molecules (i.e., when changing the methane density for different unit cells - see Figure S2). The bigger unit cells with different coverages were created by multiplying the 2×2 unit cell and removing every forth methane molecule in the system for the ones with a coverage of 25% and by removing all but one molecule in the case of the 10×10 system, creating a coverage of only 4.0%. For the 3×3 unit cell an aluminum layer with 9 surface atoms per unit cell was created. The adsorption site of the methane molecule was obtained in the same way as in the full coverage 2×2 case, namely by placing the methane molecule on the surface and fully relaxing its geometry (keeping only the positions of the Al atoms fixed). The resulting coverages are summarized in Table S1. This shows that what primarily counts for the described effect is the density of excited core holes.

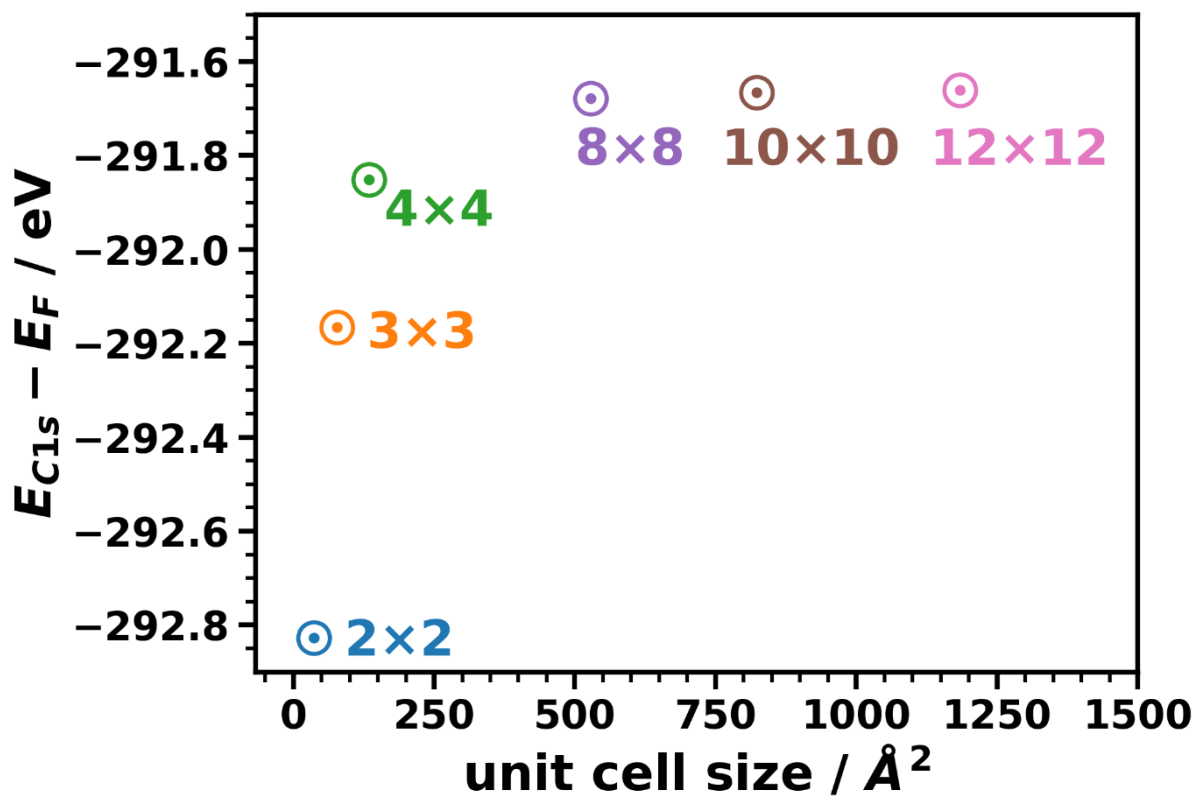


Figure S1. *C* 1s core-level binding energy of methane adsorbed on Al(100) as a function of the chosen unit cell size with different methane coverages (see Table S1). The calculations were done employing the final-state approach within the Slater-Janak transition-state approximation.

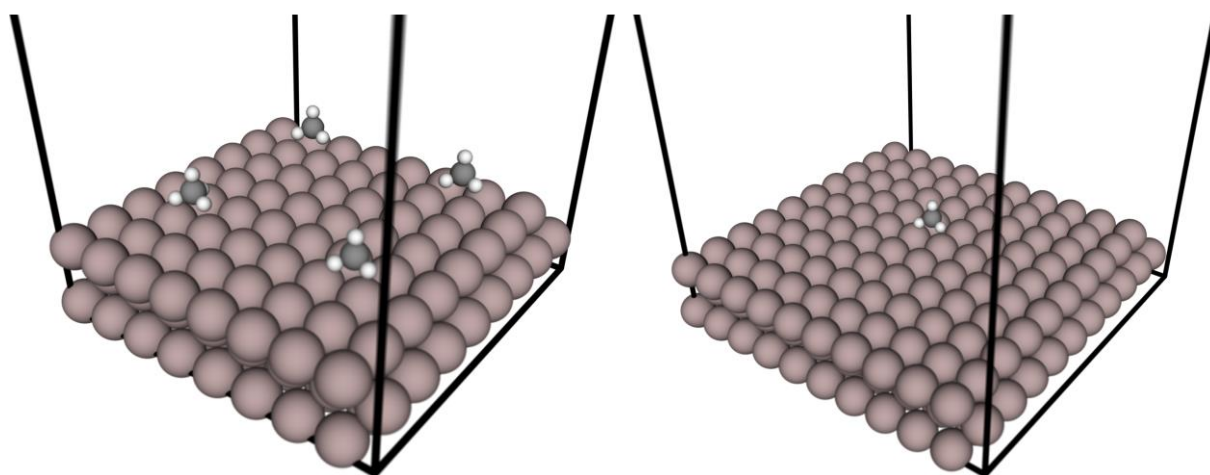


Figure S2. Left: Unit cell of the 8x8 system with a methane coverage of 25%. Right: Unit cell of the 10x10 system with a methane coverage of 4%.

Table S1. methane coverage of differently sized supercells.

Supercell size	methane density / molecules per Å ²	methane density / % of full coverage
2×2	0.0303	100.0
3×3	0.0135	44.6
4×4	0.0076	25.0
8×8	0.0076	25.0
10×10	0.0012	4.0
12×12	0.0076	25.0

2. Methodological details and tests

2.1. Information on the employed basis functions

The basis functions employed in the FHI-aims simulations have the format

$$\Phi(r) = \frac{u(r)}{r} * Y_{lm}(\theta, \phi)$$

in spherical coordinates (r, θ, ϕ) relative to a given atomic center. FHI-aims provides for every atomic species a preconstructed *species_defaults* file. The used tight basis sets were not further adjusted, because they afforded the required accuracy and efficiency. Note: If a higher tier for the basis set, i.e. when using tight settings, is used, all lower basis functions must be used as well.

Table S2. Basis functions that have been used for all calculations performed with FHI-aims¹. The abbreviations read as follows^a: $X(nl, z)$, where X describes the type of basis function where H stands for hydrogen-like functions and ionic for a free-ion like radial function. The parameter n stands for the main/radial quantum number, l denotes the angular momentum quantum number (s, p, d, f, \dots), and z denotes an effective nuclear charge, which scales the radial function in the defining Coulomb potential for the hydrogen-like function. In the case of free-ion like radial functions, z specifies the onset radius of the confining potential. If auto is specified instead of a numerical value, the default onset is used.

	H	C	Al
Minimal	valence(1s, 1.0)	valence(2s, 2.0) valence(2p, 2.0)	valence(3s, 2.0) valence(3p, 1.0)
First tier	H(2s, 2.1) H(2p, 3.5)	H(2p, 1.7) H(3d, 6) H(2s, 4.9)	ionic(3d, auto) ionic(3p, auto) H(4f, 4.7) ionic(3s, auto)
Second tier	H(1s, 0.85) H(2p, 3.7) H(2s, 1.2) H(3d, 7.0)	H(4f, 9.8) H(3p, 5.2) H(3s, 4.3) H(5g, 14.4) H(3d, 6.2)	H(5g, 7) H(H3d, 6)

2.2. Convergence of the k-point grid

The Γ -centered k-point mesh was evenly split along the reciprocal lattice vectors of the unit cell with the same number of k-points in x- and y-direction and 1 k-point in z-direction. This was done because of the quadratic unit cell and the repeated slab approach. When applying the repeated slab approach, only 1 k-point in z-direction is used, as the interface is not periodic in that direction. Due to the fact that the k-point mesh samples reciprocal space, smaller unit cells require the use of more k-points. Therefore, when the unit cell size was doubled in a given direction, the number of k-points in that direction was halved. To find the number of k-points in x- and y-direction per unit cell length, which are needed to get converged results, several calculations were done with an increasing

^a As described in the FHI-aims manual, version January 23, 2017.

number of k-points for the two smallest systems until the obtained values of interest did not change beyond a certain threshold. This procedure yielded that 400 k-points per topmost aluminum atom - i.e. 4 Al atoms at the surface in the case of the 2×2 unit cell, 16 surface atoms in the case of the 4×4 supercell, and 9 surface atoms in the case of the 3×3 unit cell - were enough to get orbital energies converged to at least ± 0.002 eV. The exact number of k-points used for each supercell and the k-point density per surface atom is shown in Table S3.

Table S3. Details on the used k-point grid for the different supercells calculated.

System name	Number of surface Al atoms in x- and y-direction	k-points in x- & y- direction	k-points in z-direction	K-points per surface atom
2×2	2	12	1	576
3×3	3	8	1	576
4×4	4	5	1	400
6×6	6	4	1	576
8×8	8	4	1	1024
10×10	10	2	1	400
12×12	12	2	1	576

2.3. Impact of the number of layers contained in the slab

Owing to the very extended supercells required for the present manuscript, all data presented in the main manuscript rely on metal slabs consisting of only three Al layers. To ensure that this is sufficient for calculating the core-level binding energies of the present system (where there is no significant substrate/adsorbate charge transfer) test calculations for the smallest 2×2 unit cell containing 6 Al layers were also performed. As can be seen in Table S4, the C 1s orbital energies for the two slab thicknesses differed by only ~ 0.01 - 0.02 eV, even in cases, where the methane atom was moved farther away from the surface slab resulting in a bigger dipole. This suggests that the consideration of three-layer slabs is sufficient for the present purpose.

Table S4. carbon 1s orbital energies calculated for the 2×2 unit cell within the Slater-Janak transition-state approach for different adsorption heights of the methane molecule on two slabs differing only in the number of aluminum layers used to represent the metal slab.

Adsorption distance	C 1s orbital energy – E _F / eV	
	3 layer slab	6 layer slab
Equilibrium	-292.83	-292.82
+1 Å	-293.10	-293.08
+2 Å	-293.16	-293.14
+3 Å	-293.15	-293.14

2.4. Impact of the geometric relaxation of the topmost metal layer

The aluminum slab was constructed with ASE², utilizing the function to create a fcc(100) surface slab with a tabulated lattice constant of 4.05 Å. To mimic the metal slab, the lowest layer of aluminum atoms was always fixed. To test whether the other layers need to be relaxed, two additional systems were calculated. One with the topmost layer and one with the two topmost layers allowed to relax during a full geometric optimization. Again, this hardly affected the core-level binding energies (see Table S5). Thus, for all calculations the slab with the aluminum atoms in the ideal bulk lattice positions was used.

Table S5. Fermi-level aligned carbon 1s orbital energies of an adsorbed methane molecule on differently geometrically optimized aluminum slabs calculated for the 2×2 system.

Relaxed Al layers of the metal slab	C 1s orbital energy – E _F / eV
none	-292.83
topmost layer	-292.81
2 topmost layers	-292.80

2.5. Spin polarized calculations

To test whether one needs to perform spin polarized calculations, selected supercells were calculated with spin unrestricted settings. Therefore, in the *control.in* file to start the FHI-aims¹ calculations, the spin parameter was set to collinear and the force_occupation parameter was set by the following lines in the case of a calculation of the 4×4 system:

```
force_occupation_projector 49 1 0.5 49 52
force_occupation_projector 49 2 1.0 49 52
```

Additionally, an initial guess for the spin of the excited atom needs to be set with the keyword `initial_moment` in the `geometry.in` file in the line following the specification of the excited carbon atom. The results obtained with unrestricted spin settings yielded the same qualitative trend (see Figure S3) as the spin restricted calculations. In fact, the mean value of the spin up and spin down orbitals is close to the energy of the C 1s orbital in the restricted calculations.

What is more relevant in the present context is, however, that the energy difference between the 2×2 and 4×4 unit cells is essentially the same for the spin up, spin down, and spin unrestricted channels (1.017 eV; 1.019 eV; 1.019 eV).

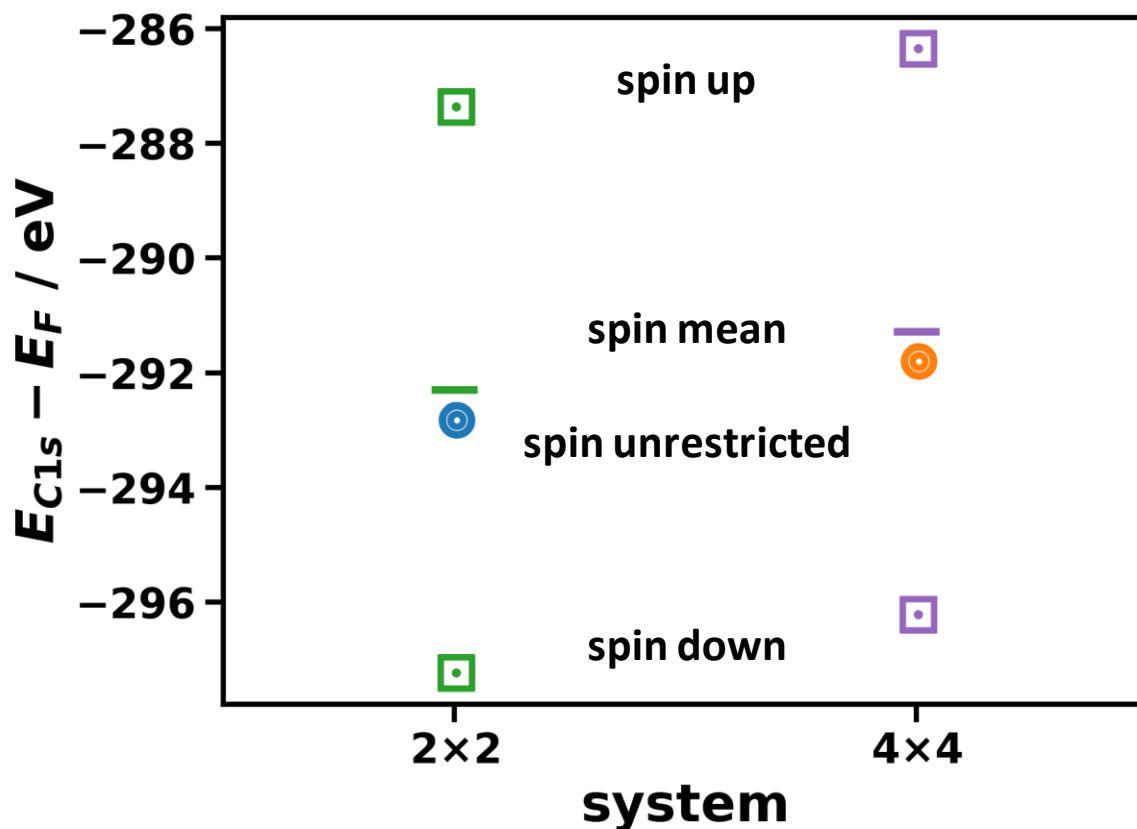


Figure S3. Carbon 1s core orbital energies calculated within the Slater-Janak transition-state theory with spin restricted, i.e. Kohn-Sham eigenvalue set to $1.5e^-$ (circles) and spin unrestricted (squares) for two different systems. Furthermore, the arithmetic mean of the spin down (occupation set to $1e^-$) and the spin up (occupation set to $0.5e^-$) eigenstate is plotted.

3. Charge rearrangements due to the excitation

When utilizing the Slater-Janak transition-state theory, half an electron is removed from the excited core hole. This charge is then placed into the lowest unoccupied orbital in the calculated system. In the case of a system with a metal substrate, as considered in this manuscript, this corresponds to a state right at the Fermi level. Notably, the region of electron accumulation following the core-level excitation is found right above the metal surface underneath the excited molecule, as shown in Figure S4. Please note that the blue feature in Figure S4 in the region of methane is a consequence of electron depletion due to the polarization of the molecule. Consequently, there is one excitation per supercell and the excitation density is inversely proportional to the size of the chosen supercell.

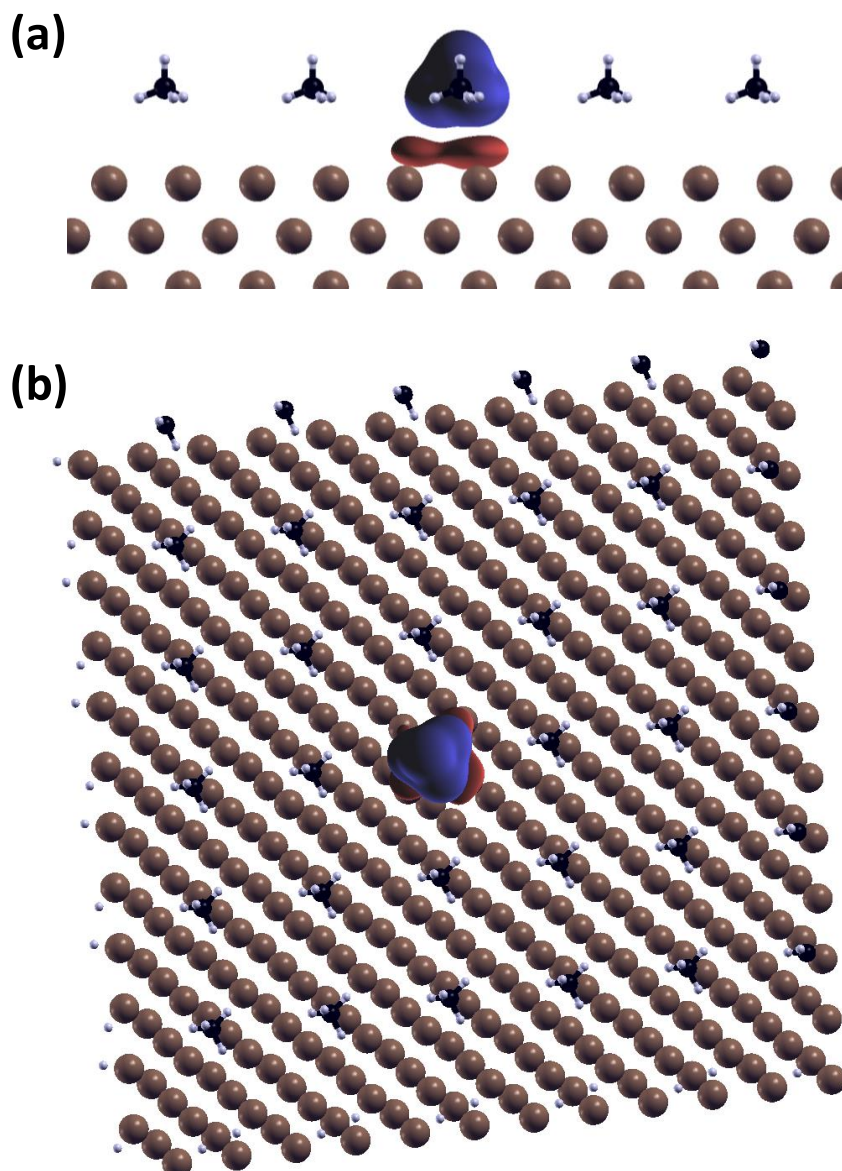


Figure S4. Isodensity plot – front view (a) and top view (b) of the 12×12 supercell showing the electron depletion (blue) and accumulation (red) due to the removal of half an electron from the carbon $1s$ orbital of the excited molecule. This charge is moved to the lowest unoccupied level in the system by FHI-aims. As can be seen this is localized directly underneath the excited molecule.

3.1. Plane-integrated charge rearrangements

Notably, the shapes of the calculated plane-integrated charge rearrangements are independent of the supercell size (cf., data for the 4×4 and 12×12 cells), with minor deviations for the smallest 2×2 cell (solid blue line in Figure S5). The latter we attribute to a somewhat different electronic structure in the 2×2 case, in which all adsorbate

molecules are excited. In contrast, in the calculations of larger cells the excited methane molecule is surrounded by inequivalent molecules (i.e., by molecules in their electronic ground state), which minimizes hybridization effects between the molecules. This aspect will be discussed in more detail later, when discussing Fermi-level pinning effects.

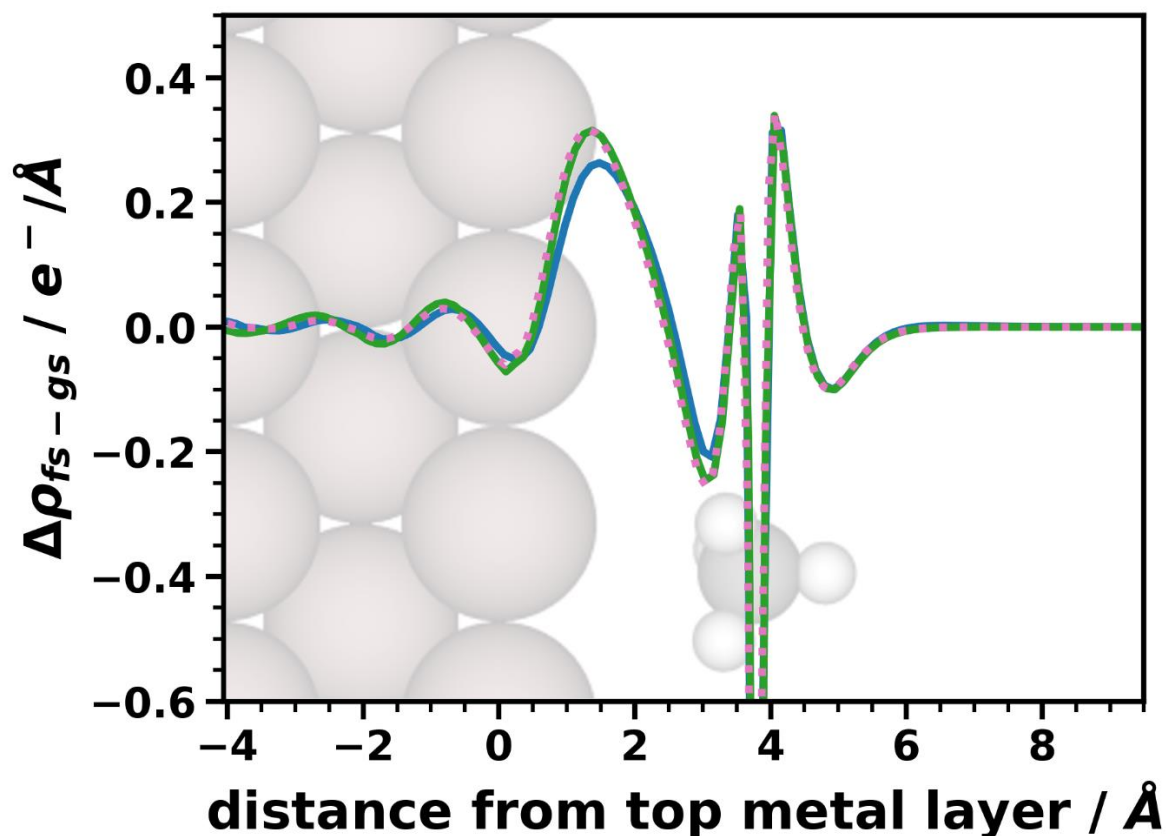


Figure S5. Charge rearrangements between the initial- and final-state calculation, $\Delta\rho_{fs-gs}$, integrated over the unit cell for the 2×2 (blue, solid line), 4×4 (green, solid line), and 12×12 (pink, dotted line) surface supercell as a function of the adsorption height. The 4×4 and 12×12 data lie exactly on top of each other and the 2×2 data deviate only weakly, especially next to the metal surface.

3.2. Plane integrated rearrangements as a function of the adsorption distance

In the previous section we show the charge rearrangements ($\Delta\rho_{fs-gs}$) in final-state calculations relative to the ground state charge density for different excitation densities (cf. Figure 5). Here we show the charge rearrangements due to different adsorption

heights. As can be seen in Figure S6 the charge density difference in and right above the metal slab stays largely the same, no matter how far away the excited methane molecules are moved away from the substrate. Furthermore, the qualitative (and quantitative) charge rearrangements at the molecule prevail, when it is moved away from the metal slab.

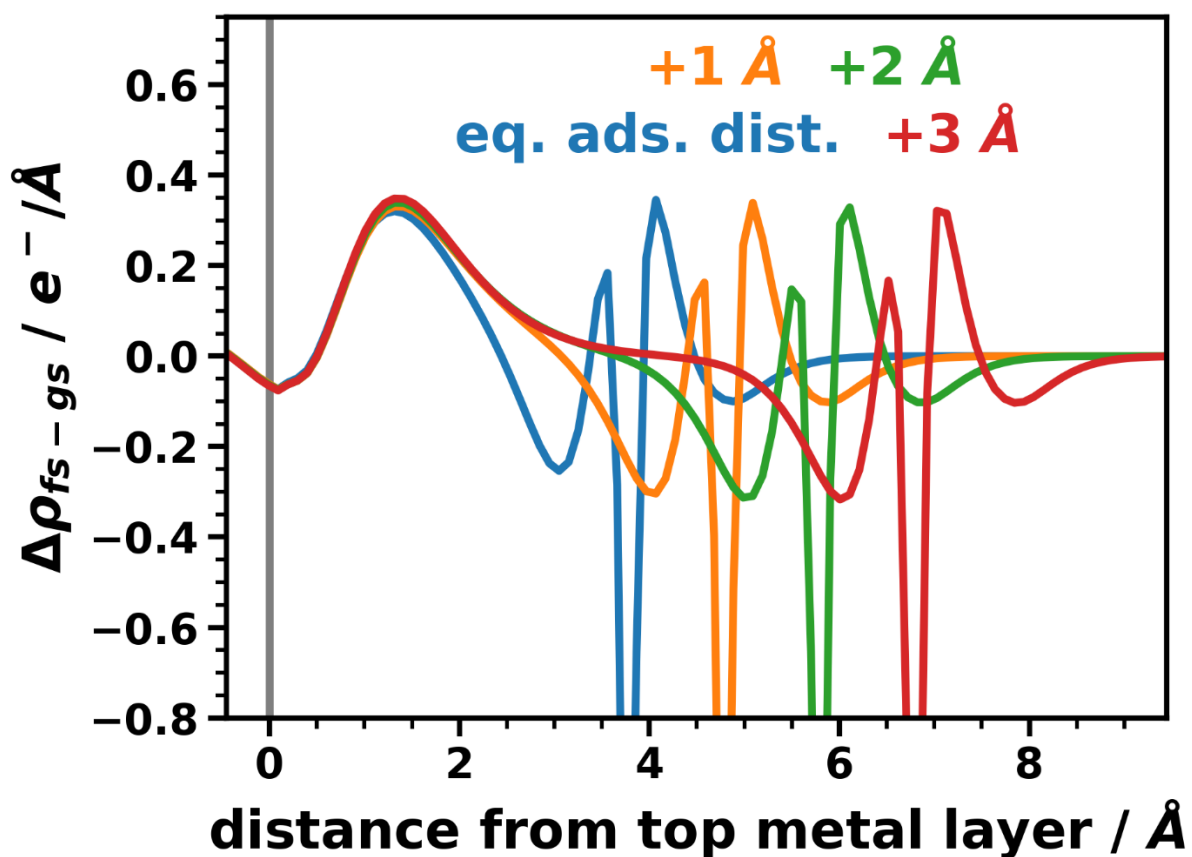


Figure S6. Plane-integrated charge rearrangement due to the excitation - i.e. difference of the charge density of the final-state and the ground state calculation - for different adsorption heights of the methane molecule, calculated for the 10×10 supercell in units of the electron charge. Negative values mean electron depletion and positive values electron accumulation. The grey line indicates the position of the topmost aluminum layer.

3.3. Cumulative charge rearrangements as a function of the adsorption distance

Figure S7 shows the integral of $\Delta\rho_{fs-gs}$ (the quantity plotted in Figure S6) over the z coordinate of the unit cell as a function of the position up to which the integration has

been performed. This integral can either be interpreted as a quantity proportional to the electric field resulting from $\Delta\rho_{fs-gs}$, or, more useful in the present context, as ΔQ_{fs-gs} , the cumulative charge rearrangement, which quantifies, how many electrons have been transferred from below to above a plane at position z due to the excitation. Figure S7 shows that the maximum cumulative charge rearrangement somewhat increases with increasing adsorption height, which we attribute to the fact that at larger adsorption distances the overlap between the screening charges in the metal and the polarization charges in the adsorbate diminishes. This observation explains, the slightly superlinear increase of $\Delta E_{C_{1s}}$ with adsorption distance observed in Figure 6b.

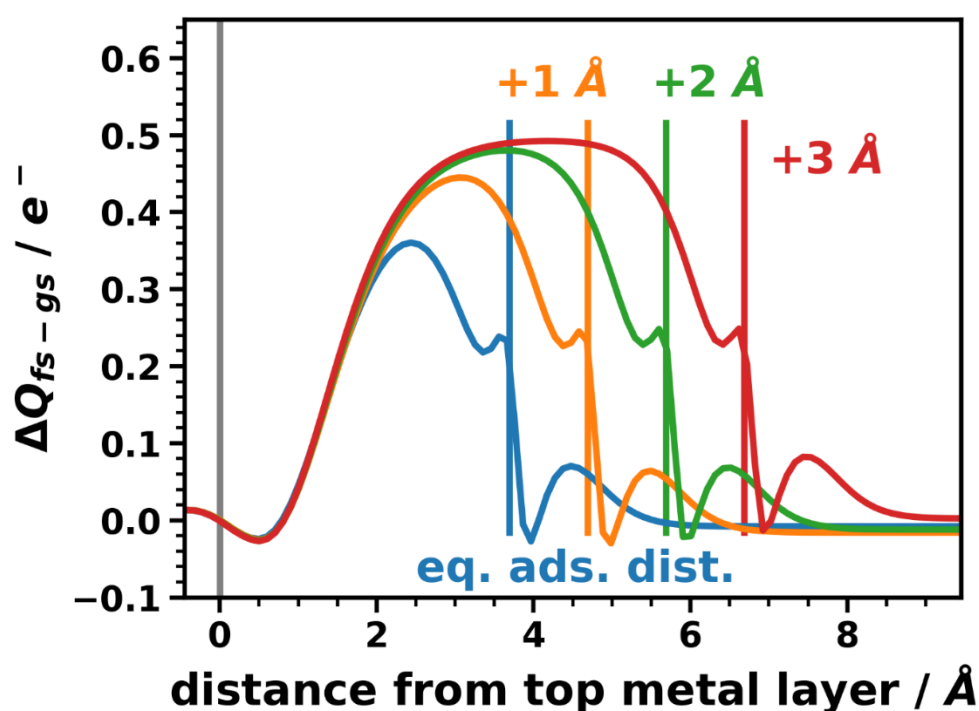


Figure S7. Cumulative charge rearrangement due to the excitation – i.e. integrated difference of the charge density of the final-state and the ground state calculation (see Figure S6) – for the 10×10 supercell for different adsorption heights of the methane molecules. The grey line indicates the position of the topmost aluminum layer and the blue, orange, green and red line represent the position of the carbon atom of the methane molecule in equilibrium position, and moved farther away by 1, 2, and 3 Å, respectively.

4. Shift of electronic levels

Due to collective electrostatic effects arising from the artificial dipole array in the calculations, all electronic states in the adsorbate layer are shifted relative to the Fermi level of the substrate.

4.1. Work function shifts

As a result of collective electrostatic effects, also the work function is shifted depending on the supercell size, i.e. the excitation density. The impact of this shift on the work function is inversely proportional to the base area of the supercell. In Figure S8 the work function change due to the artificial dipole layer in the final-state calculation is plotted over the inverse supercell size. As one can see all datapoints are essentially linear with the exception of the 2×2 unit cell, for which the evolution becomes sublinear. This is due to depolarization effects³⁻⁸.

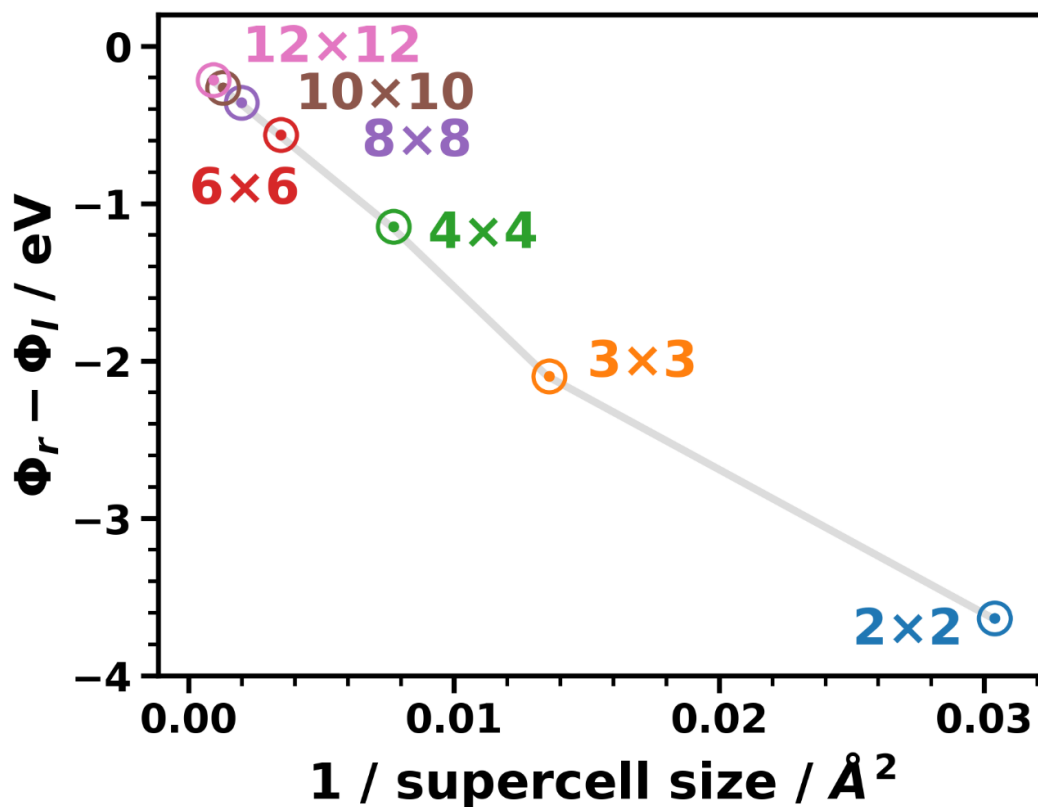


Figure S8. Work function change of methane adsorbed on an Al(100) slab as a function of the inverse supercell size for calculations employing the final-state approach within the Slater-Janak transition-state approximation.

4.2. Electrostatic model for estimating work-function changes

Starting from the Helmholtz solution to the Poisson equation one obtains the following numerical relation between Φ , the work function including the artificial dipole layer, Φ_0 , the work function in the electronic ground state, $Q \cdot \Delta z$, the dipole moment of one dipole (expressed via the transferred charge, Q , and the charge-transfer distance, Δz), ϵ_r , the dielectric constant of the organic layer, and A , the area per dipole:

$$\Phi = \Phi_0 - \frac{q_e Q \cdot \Delta z}{\epsilon_0 \epsilon_r A}$$

Here q_e is the charge of an electron and ϵ_0 is the vacuum permittivity. When providing energies in eV, lengths in Å, areas in Å², and Q in multiples of the elementary charge, the following numerical value equation is obtained (with 180.92 being a unit-conversion factor):

$$\Phi = \Phi_0 - 180.92 \frac{Q \cdot \Delta z}{\epsilon_r A}$$

In the case of Slater-Janak transition-state calculations, Q is set to 0.5 times the elementary charge. For the system discussed in the present manuscript, Δz amounts to 2 Å as the approximate distance over which the potential drops in Fig. 4b, and ϵ_r is set to 1.5 (to account for screening effects within the methane layer).

4.3. Carbon 1s core-level binding energies

Furthermore, also the core-level binding energies are shifted. The magnitude of that shift again depends on the dipole density, i.e. the excitation density, which is inversely proportional to the size of the supercell. In Figure S9 the core-level energies are plotted over the inverse supercell size. As one can see, in this case an essentially linear relation is obtained. The “linearity” condition is, however, less well fulfilled than for the work-function change. We attribute this to the “locality” character of the core-level shifts, i.e.,

the fact that for core-level binding energies also lateral variations in the electrostatic energy are highly relevant.

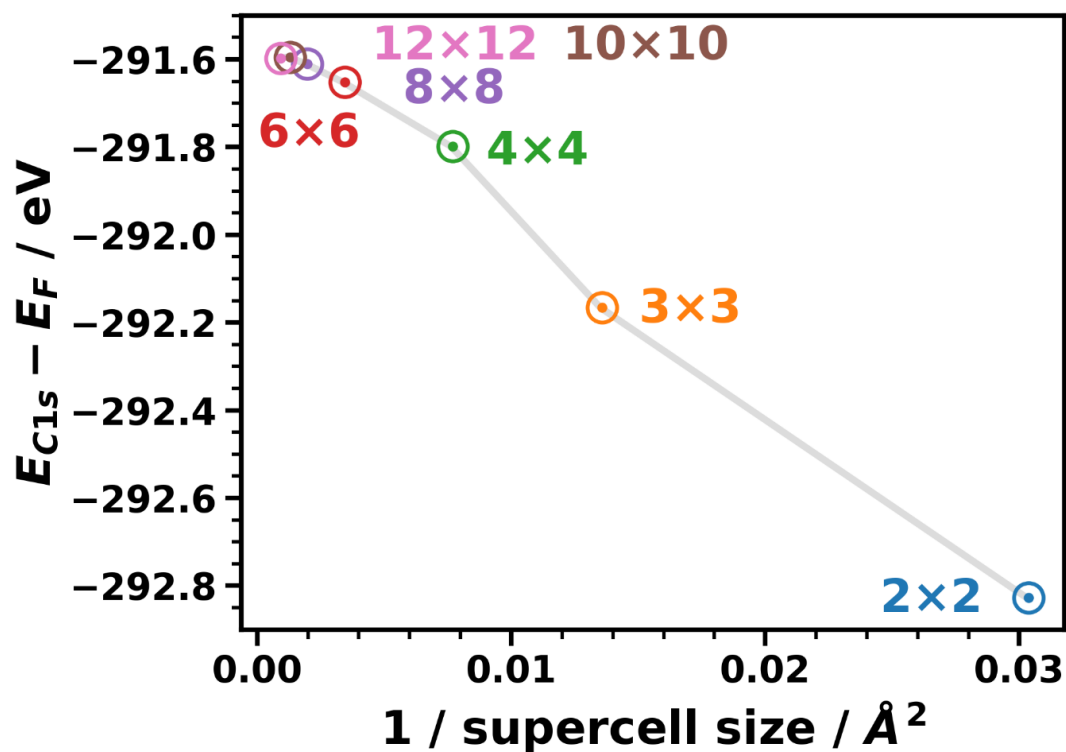


Figure S9. Carbon 1s core-level binding energy of methane adsorbed on an Al(100) slab as a function of the inverse supercell size for calculations employing the final-state approach within the Slater-Janak transition-state approximation.

5. Half core-hole vs. full core-hole calculations

If the observed shifts of the calculated core-level binding energies are indeed a consequence of electrostatic effects, their magnitude should depend linearly on the amount of transferred charge moved from the C 1s orbital to the Fermi level, i.e. to the metal's surface. This means in the case of a full core-hole calculation, the shift of the orbital energies should be twice as large as in calculations where half an electron is removed from the core orbital. Such a linear increase can indeed be observed, as shown in Figure S10 (at least as long as no Fermi-level pinning occurs, as discussed in chapter 10 of this Supporting Information).

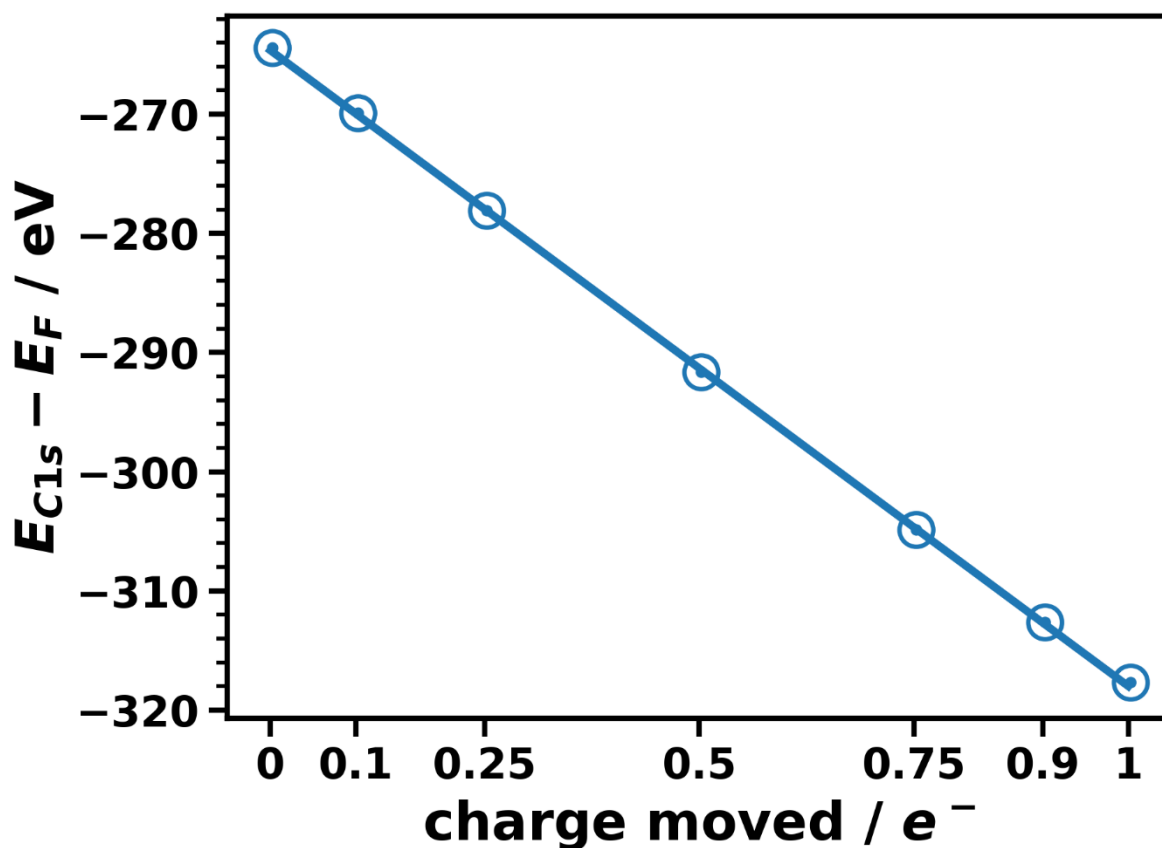


Figure S10. Carbon 1s orbital energies for different amounts of charge moved from the core level to the lowest unoccupied level of the 8×8 supercell, and a linear fit. Zero charge transfer corresponds to a ground state calculation and a transfer of 0.5 electrons represents Slater's transition-state theory. The other points were calculated to show that this shift depends linearly on the transferred charge.

6. Final-state calculations relying on the Δ SCF approach

Figure S11 compares the carbon 1s orbital energies calculated with two different final-state methodologies, namely the Slater-Janak transition-state theory and the Δ SCF method. In the former, half an electron is removed from the core hole and placed in the lowest unoccupied orbital of the system (in this case at the Fermi level, i.e. somewhere at the metal's surface) and in the latter a full electron is removed from the core orbital and in our case placed into the lowest unoccupied orbital. In the Δ SCF method, the core-level binding energies are then associated with the energy differences of the systems in their

excited and ground state, respectively. For all but the smallest unit cell, the core-level binding energies obtained with the two different methodologies are essentially rigidly shifted relative to each other. This shows that the artificial collective electrostatic shifts are similar for both methods. This is insofar intriguing, as the artefacts play out differently in the two approaches: When applying the Slater-Janak transition-state theory, the collective electrostatic shifts directly affect the energetic positions of the C 1s orbitals relative to the Fermi energy. Conversely, in the Δ SCF method they manifest themselves as the “charging energy” of an interfacial capacitor (cf. main manuscript).

The only exception from the overall trend is the 2×2 unit cell, for which the C 1s core-level binding energy calculated within the Δ SCF approach is shifted significantly less than when applying the Slater-Janak transition-state theory. The reason for that is Fermi-level pinning similar to the effects observed in Figure 5a of the main manuscript. The reason why Fermi-level pinning for the Δ SCF approach occurs already at the equilibrium distance, while in Figure 5a it occurs especially for larger distances is the increased amount of charge transfer in the Δ SCF (a full electron instead of half an electron), which results in an increased dipole density.

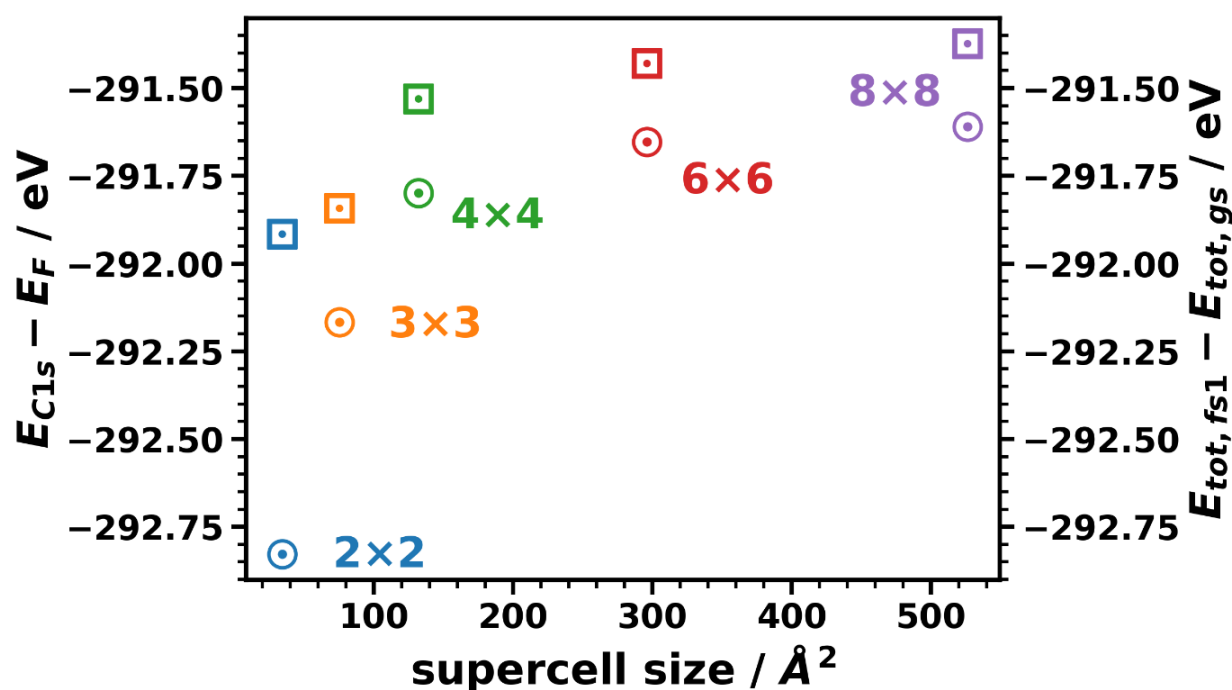


Figure S11. C 1s core-level binding energies calculated within the Slater-Janak transition-state theory (circles) and by applying a Δ SCF approach (squares) for varying supercell sizes and excitation densities.

7. Impact of the core-hole excitations on the work function on the Al-side of the slab

Due to the nature of final-state calculations, where charge is moved from the core orbital of an adsorbate to the lowest unoccupied level of the system, i.e., in this case to the metal slab, it is necessary to check that the latter does not deteriorate the description of the electronic structure of the substrate. To test that, we calculated to what extent the work function at the bottom side of the metal slab (i.e., the side not covered by the adsorbate) is affected by the added charge. This is done for different supercell sizes (and, thus, excitation densities). The results shown in Table S6 confirm that in none of the considered cases the bottom-side work function is changed significantly, further confirming the notion that the 3-layer Al slab is sufficiently thick for the studies reported in the present manuscript.

Table S6. Left (aluminum-side) and right (adsorbate-side) work function of the system calculated within the final-state approach for different supercells.

Supercell size	$\Phi_{\text{Left}} / \text{eV}$	$\Phi_{\text{Right}} / \text{eV}$
2×2	4.32	0.69
3×3	4.37	2.27
4×4	4.40	3.25
6×6	4.39	3.83
8×8	4.40	4.04
10×10	4.41	4.14
12×12	4.40	4.19

8. Impact of locality effects of the electrostatic energy on core-level binding energies

Here we show quantitatively that for properly capturing the impact of collective electrostatics on core-level shifts, one has to average the electrostatic energy over much smaller areas than the cross-section of the unit cell. Correspondingly, Figure S12 shows the electrostatic energy averaged over an area of only 0.08 \AA^2 parallel to the surface (as an estimate for the “extent” of a C 1s orbital; see section 8.1) for the 2×2 and 12×12 cells. Both graphs reveal the pronounced dip in electrostatic energy around the core hole. Far enough above the methane molecule, the averaged electrostatic energy gradually approach the far-field values, like in Figure 3b, albeit at a much slower rate. The latter is fully consistent with the data in Figure 4. A disadvantage of the way the data are plotted in Figure S12a is, however, that the massive drops in the energy around the carbon atoms obscures the differences between different excitation densities.

Thus, in Figure S12b we plot the difference between the two curves contained in Figure S12a. Then, the 12×12 supercell can be viewed as the situation in the absence of artificial collective electrostatic effects (due to the highly diluted dipole density), while these effects are maximized for the 2×2 cell. Consequently, this plot illustrates their impact on a lateral length-scale consistent with the extent of the C 1s electron. In this way it accounts for the local nature at which core-level excitations probe the electrostatic landscape. From these data one learns that the artificial shift in electrostatic energy at the position of the C atom is, indeed, way smaller than the shift of the energy far above the interface. This reconciles the data from Figures 2a and 3c. In particular, it confirms the notion that the different magnitudes of the artificial shifts of the core-level binding energies (in Figure 2) and the work-function changes (in Figure 3c) solely arise from different “locality” with which these quantities probe the electrostatic energy across the interface.

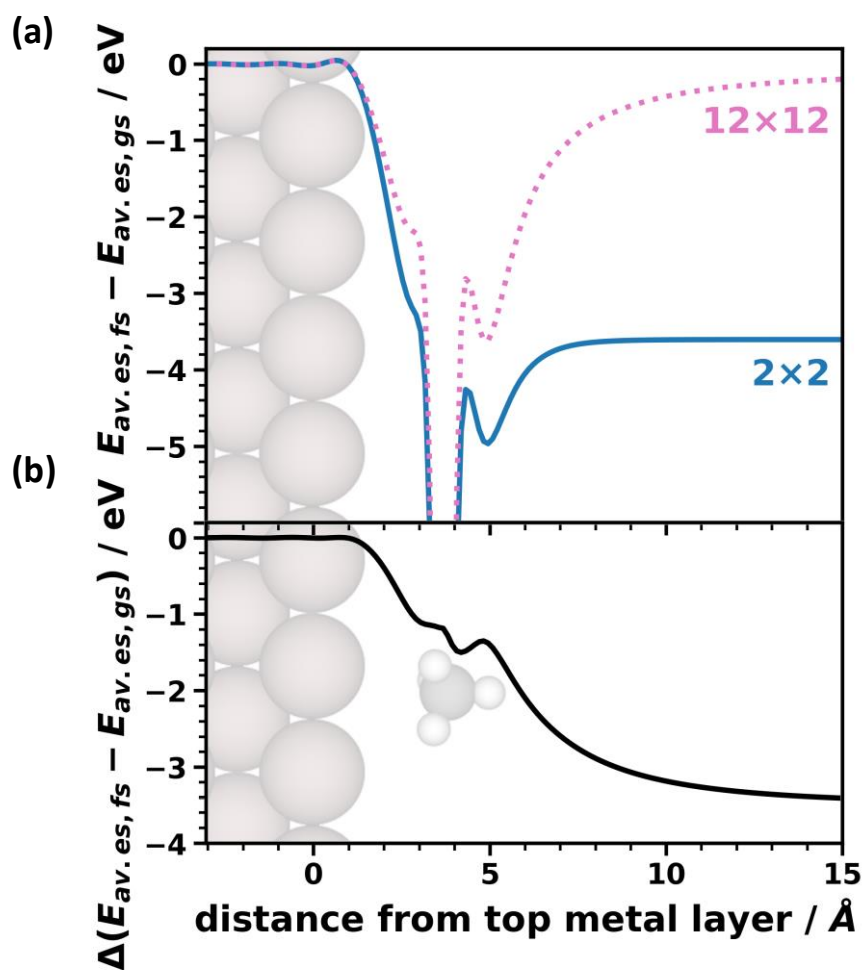


Figure S12. (a) Difference in electrostatic energy between final-state and ground state calculations averaged over quadratic areas of $0.286 \text{ \AA} \times 0.286 \text{ \AA}$ parallel to the substrate surface for the 2×2 (blue, solid) and 12×12 (pink, dotted) supercells. The average electrostatic energy is plotted as a function of the distance from the topmost metal layer and the area over which is averaged is chosen such that at the adsorption distance of the methane molecules, the excited carbon atom lies at the center of the square. (b) Difference of the data in panel (a) between the 2×2 and 12×12 unit cells. As the 12×12 supercell represents an essentially isolated excited dipole, these data characterize the change in the local electrostatic energy due to the surrounding excited dipoles for the 2×2 cells. In this context it is important to point out that the general shape of the curve in this figure does not depend on the specific area over which the electrostatic energy is averaged (as long as it is small enough). This is shown in the next section.

8.1. Dependence of evolution of the local electrostatic energy on the size over which the lateral averaging occurs

To approximate electronic wavefunctions, Slater proposed the use of hydrogen-like orbitals with an effective nuclear charge. He also compiled rules for acquiring the effective nuclear charge (Z_{eff}) that should be used to take the screening of the core electrons into account. For a carbon 1s orbital this effective nuclear charge is $Z_{\text{eff}} = 5.7$,⁹ which results in a radius of $\sim 0.16 \text{ \AA}$ within which $2/3$ of the C 1s charge density are contained. From this an effective cross-sectional area of the C 1s orbital of 0.08 \AA^2 can be estimated analogous to the area used in the main manuscript (although there, for technical reasons, the averaging occurs over square voxels). In fact, when calculating the plane-averaged charge density associated with the C 1s orbital in the actual interface (see Figure S13) a consistent value is obtained.

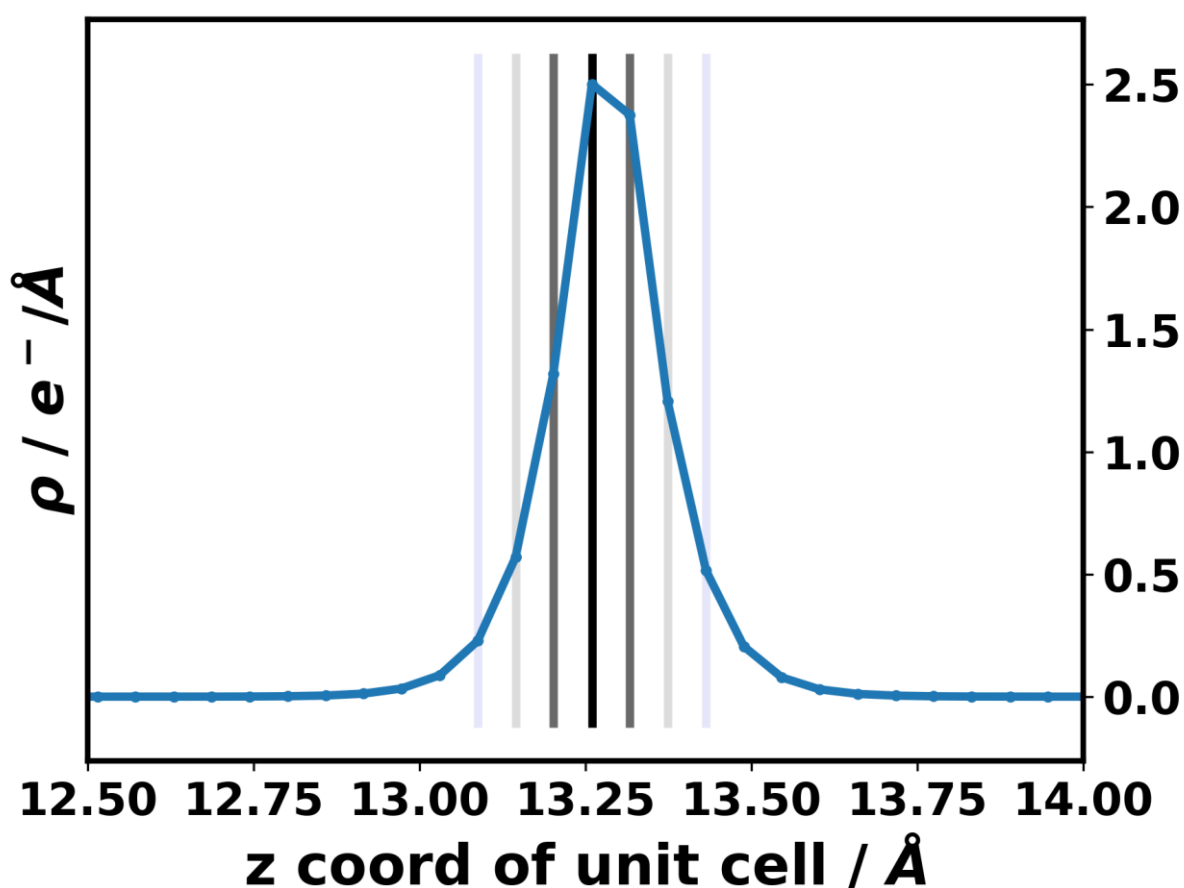


Figure S13. Plane averaged charge density of the C 1s orbital. The vertical grey lines indicate the extent of the voxels of the grid on which the charge density was written out.

The exact size of the area over which the electrostatic energy is averaged is, however, only of minor relevance: As shown in Figure S14 the depth of the potential well associated with the core hole, as expected, depends strongly on the area over which the averaging occurs. The actually relevant quantity, namely the difference in averaged potentials for the 2×2 and 12×12 supercells shown in Figure S15 is, however, not affected significantly.

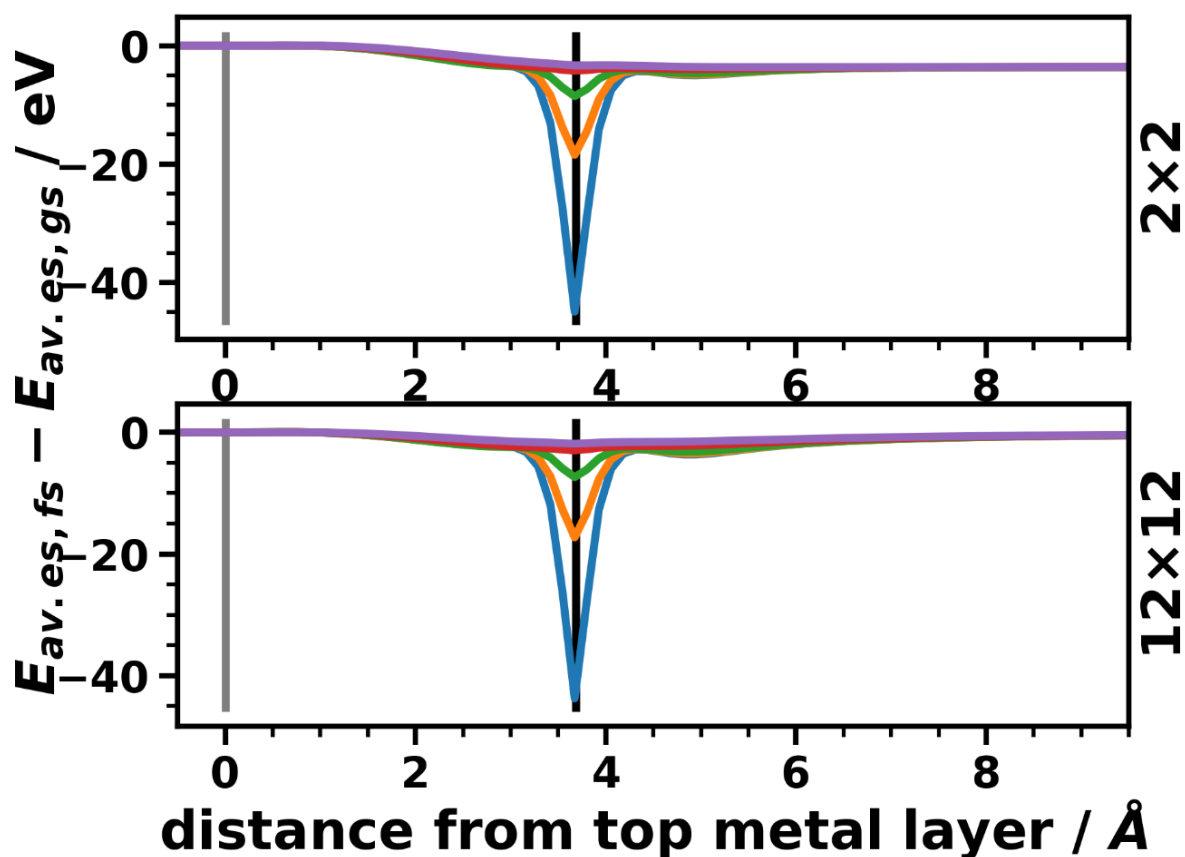


Figure S14. Electrostatic energy averaged over differently sized areas for the 2×2 (top part) and the 12×12 (bottom part) supercell. Areas plotted: blue: 0.03 \AA^2 , orange: 0.40 \AA^2 , green: 1.45 \AA^2 , red: 12.20 \AA^2 , violet: 32.15 \AA^2 (representing the total area of the 2×2 unit cell). The grey line indicates the position of the topmost aluminum layer and the black one shows the position of the carbon atom.

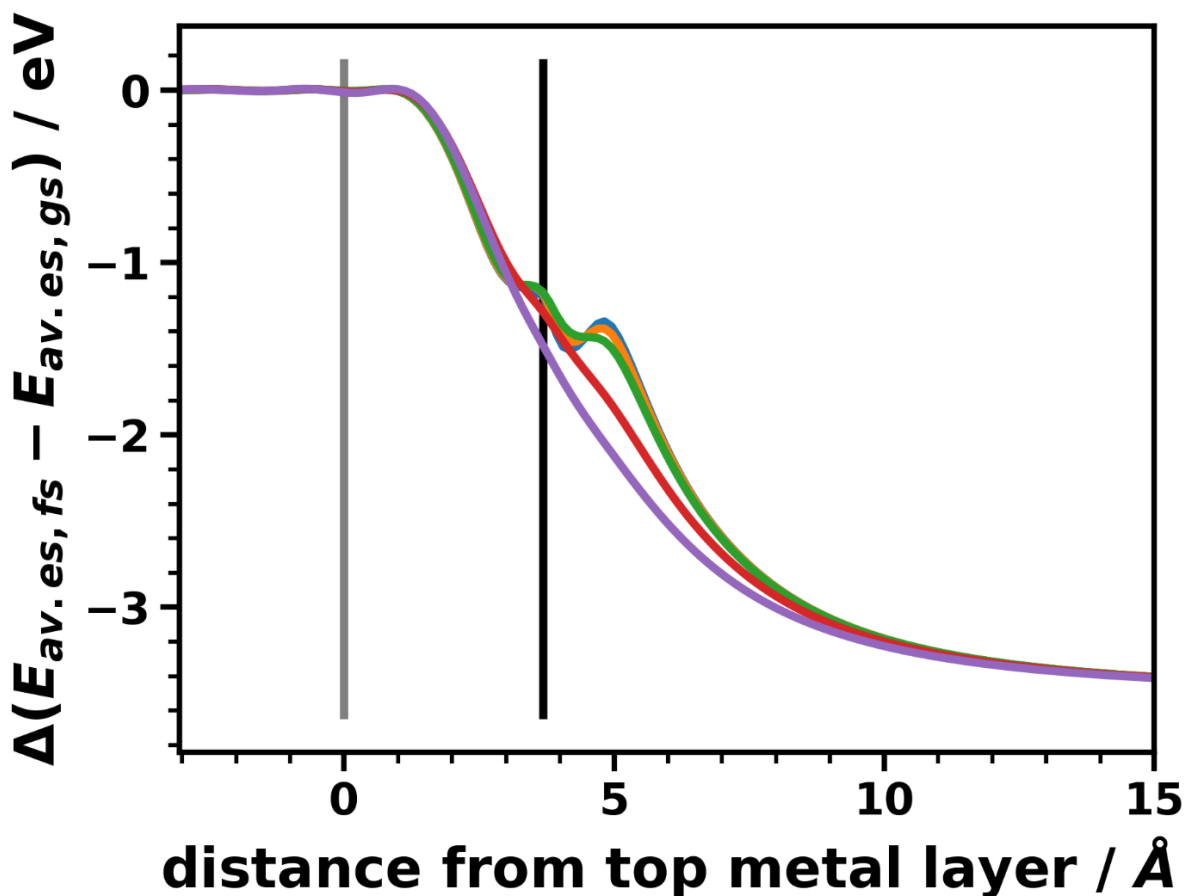


Figure S15. Difference of the averaged electrostatic energy between the 2×2 and 12×12 supercells plotted for differently sized areas over which was averaged. Areas plotted: blue: 0.03 \AA^2 , orange: 0.40 \AA^2 , green: 1.45 \AA^2 , red: 12.20 \AA^2 , violet: 32.15 \AA^2 (representing the total area of the 2×2 unit cell). The grey line indicates the position of the topmost aluminum layer and the black one shows the position of the carbon atom.

9. Fermi-level pinning for large adsorption heights and small unit cells

As can be seen in Figure 5a of the main manuscript, for the 2×2 unit cell, the adsorption distance has hardly any impact on the C 1s energies. Conversely, for the 3×3 unit cell upon increasing the adsorption distance the orbital energies are shifted up to a certain value (significantly more negative than for the 2×2) and then pin. In other words, the pinning

occurs not only at different distances, but also at very different energies. I.e., a priori, it is not clear, why the core-level in the 3×3 unit cell and in larger supercells can get shifted to energies that are significantly more negative than the energy at which pinning already occurs in the 2×2 unit cell. We here propose differences in orbital hybridization as the explanation for this effect.

Figure S16 shows the occupied and unoccupied density of states (DOS) for the 2×2 unit cell at the equilibrium adsorption distance for the ground state and for the final-state calculations. Here we also plot the unoccupied density of states at energies higher than the vacuum level above the adsorbate layer (indicated by colored vertical lines in the following plots). A priori the corresponding states cannot be properly described by an orbital-centered basis set. Nevertheless, we include it here, as it still allows the assessment of similarities between different systems (prone to the same inaccuracies due to the basis set).

The data in Figure S16 show to relevant aspects: First, the unoccupied states hybridize and broaden much more strongly than the occupied ones (as can be understood from the particularly delocalized character of the LUMO of methane shown in the top panel of Figure S16). Secondly, in the final-state calculations, in which every methane molecule is excited, the DOS is shifted essentially rigidly to higher binding energies by ~ 4.6 eV. As a consequence, the unoccupied DOS is shifted to the Fermi level and pinning occurs. Therefore, increasing the charge-transfer distance hardly changes the shift, as is shown for the unoccupied DOS of the 2×2 unit cell in Figure S17. Notably, also the shape of the unoccupied DOS hardly changes upon moving the molecules further away from the surface, indicating that the broadening of the unoccupied DOS in the 2×2 unit cell is really a consequence of inter-molecular (rather than molecule-substrate) interactions.

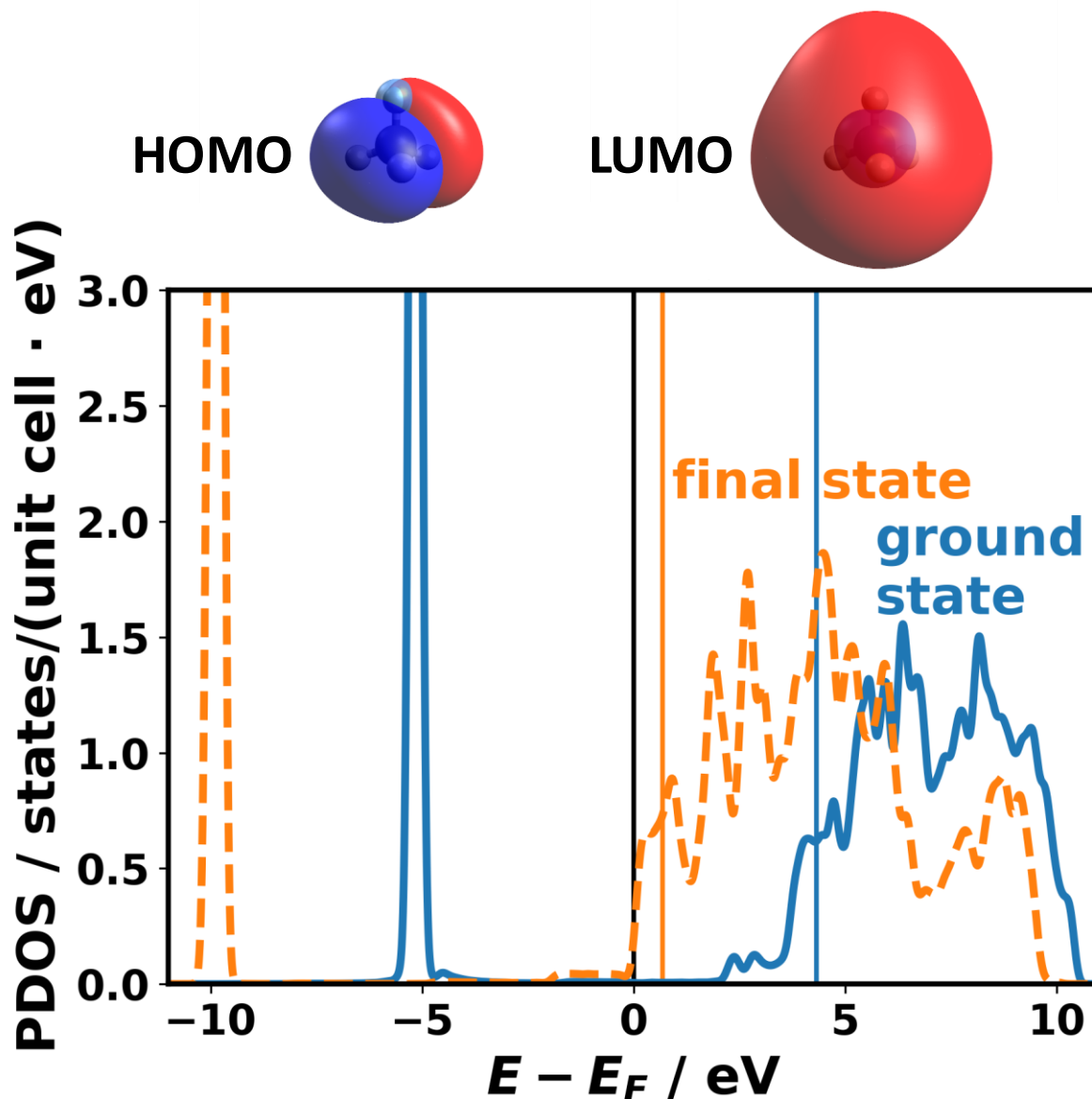


Figure S16. Occupied and unoccupied projected density of states (PDOS) of the methane molecule, adsorbed at equilibrium distance and calculated utilizing the 2×2 unit cell. The solid, blue line is the PDOS of the ground state and the orange, dashed line the PDOS of the final-state calculation. The black line indicates the Fermi level and the orange and blue lines indicate the vacuum level of the final-state and ground state calculations, respectively, above the adsorbate layer. Note that the states above the vacuum level are not correctly described with the employed basis set, but are still included for the sake of comparison. The top panel shows isodensity representations (isodensity value of 0.02 eV) of the highest occupied (HOMO) and lowest unoccupied molecular orbitals (LUMO) of a methane molecule calculated using gaussian16/RevA.03¹⁰ employing the PBE functional and a 6-311G(d,p) basis set.

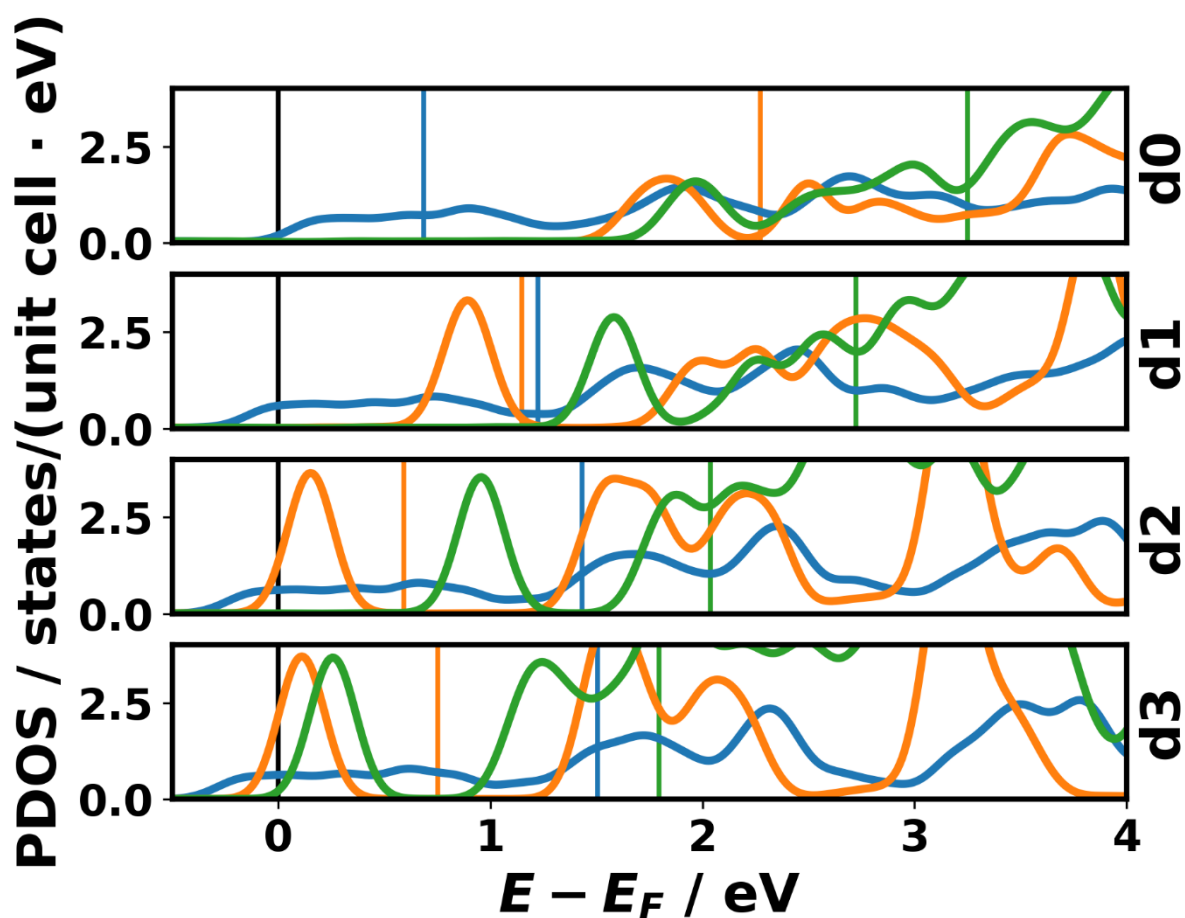


Figure S17. Density of states of the methane monolayer calculated for different adsorption heights with different supercells. The 2×2 (blue) system is pinned already at the equilibrium adsorption distance, whereas the 3×3 (orange) methane peaks shift up to the Fermi level (from d2 on). The 4×4 methane DOS is also shifted, in the case of moving the molecule 3 Å farther away from the equilibrium adsorption distance (d3) right to the Fermi level. The black line indicates the Fermi level and the orange, blue, and green lines indicate the vacuum level following the aforementioned color code. Note that the states above that vacuum level are not correctly described with the employed basis set, but are still included for the sake of comparison.

The situation is fundamentally different for the larger supercells. Starting from the 4×4 supercell, every excited molecule has only molecules in the ground state as nearest neighbors. Still, the orbitals of the excited molecules are stabilized by the electrostatic

potential of the dipoles (albeit to a lesser degree than for the 2×2 case). Due to this shift, the unoccupied orbitals of the excited molecules would still be the ones that could cause pinning. Another consequence of the shift is, however, that, energetically, they come to lie below the orbitals of the surrounding molecules, as shown by projected densities of states in Figure S18 for the 4×4 supercell. This effectively reduces the coupling between neighboring molecules and, consequently, the DOS feature that is shifted towards E_F for all larger unit cells is a rather sharp peak, as shown in Figures S17 and S19 (with the effect particularly well visible for the 4×4 cell at larger distances).

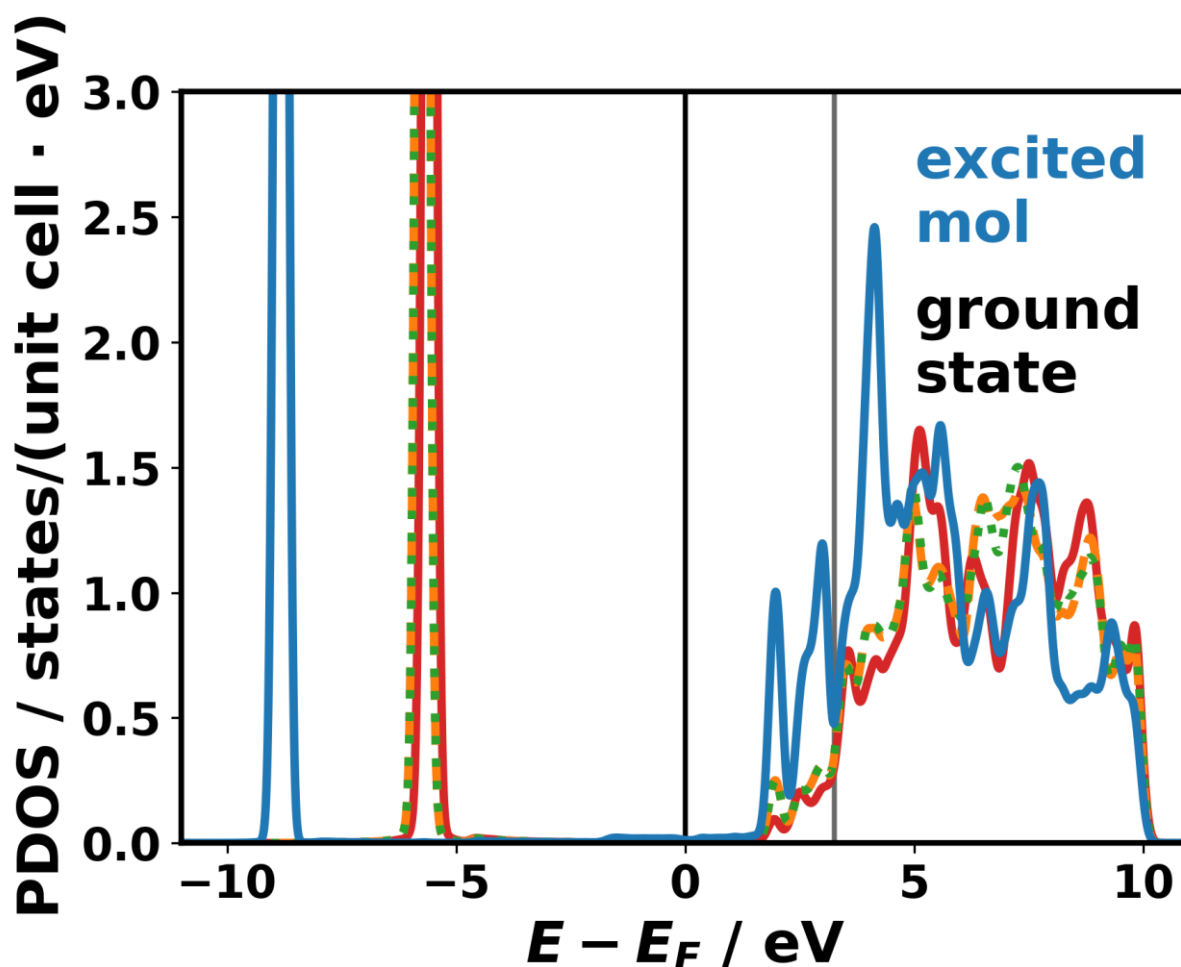


Figure S18. Density of states of the 4×4 supercell with one molecule excited projected onto the four contained methane molecules. The PDOS of the excited methane molecule is plotted as a solid, blue line. The PDOSes of the three non-excited molecules are plotted in orange, green, and red, respectively. An analysis of the less broadened, occupied DOS reveals that the features associated with the excited molecule are typically shifted by 3.1 eV. The black line indicates the Fermi level and the grey line indicates the vacuum level above the adsorbate

layer following the aforementioned color code. Note that the states above that vacuum level are not correctly described with the employed basis set, but are still included for the sake of comparison.

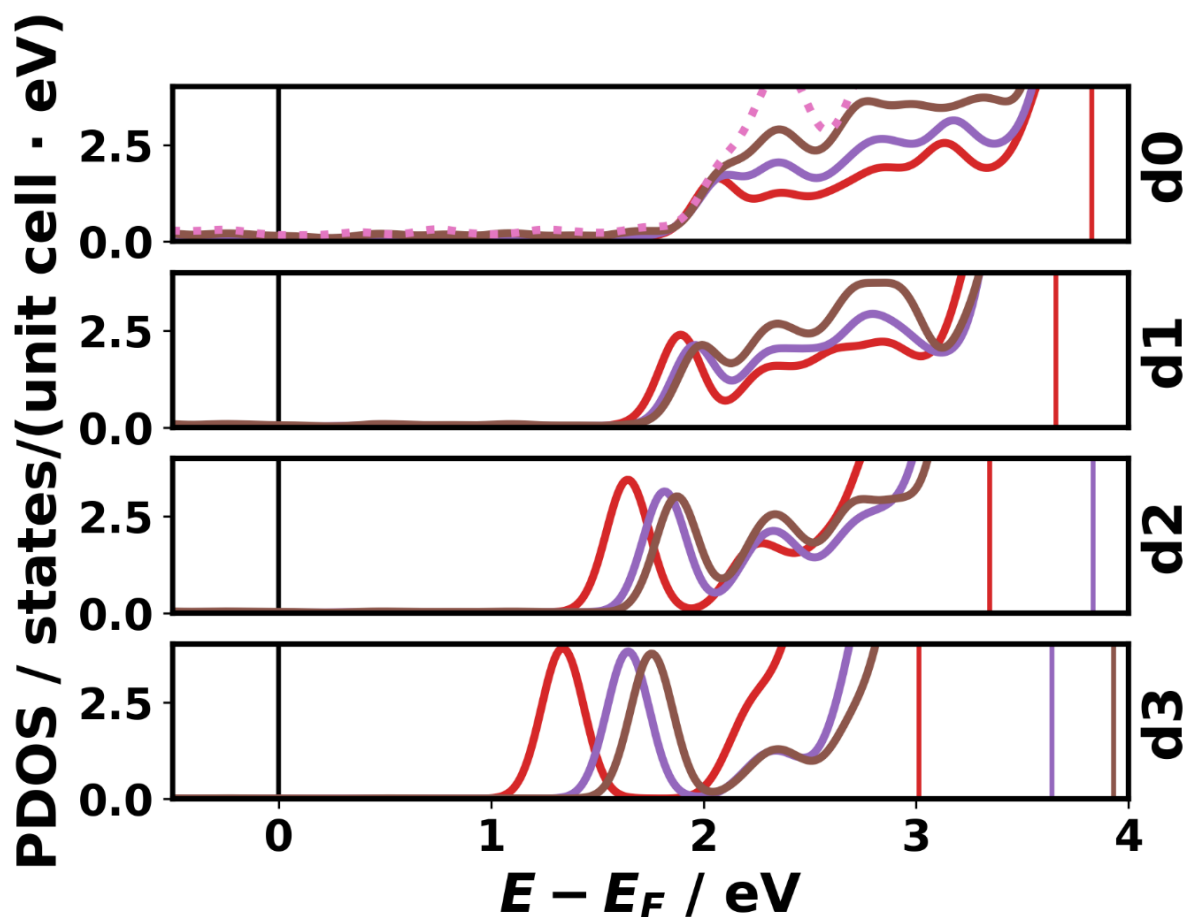


Figure S19. Density of states of the 6×6 (red), 8×8 (violet), 10×10 (brown) and 12×12 (pink dotted, only at equilibrium distance) supercell. The methane DOS shifts also in the case of the bigger supercells plotted in this figure, but not as far as in the case of the smaller supercells. The black line indicates the Fermi level and the red, violet, and brown lines indicate the vacuum level accordingly to the before mentioned color codes. The higher-lying orbitals are not properly described with the employed basis set.

10. HOMO – LUMO gap

Several test calculations were done with FHI-aims, Gaussian v16¹⁰ and VASP v5.4.4¹¹⁻¹⁴ to understand the impact of the choice of the basis set on the energies of the frontier orbitals and on the gap. The results of these tests are shown in the following table. The data show that the energies of the LUMO (and correspondingly also the value of the gap) vary somewhat with the chosen basis set, with the LUMO in the FHI-aims simulations using the tight basis set (see section 2.1) significantly lies below that of all Gaussian calculations disregarding diffuse basis functions and somewhat above the values obtained with Gaussian including diffuse basis functions as well as with VASP and a plane-wave basis set. These data suggest that pinning at the LUMO would occur at somewhat higher fields in final-state calculations using FHI-aims with a tight basis set compared to equivalent simulations using a plane-wave basis in VASP. The effect is, however, not particularly strong and by no means changes the qualitative picture.

Table S7. Highest occupied molecular orbital (HOMO) and lowest unoccupied molecular orbital (LUMO) energies and their respective band gap calculated with different methodologies and basis sets applying open (OBC) and periodic boundary conditions (PBC). For the simulations of a single molecule with FHI-aims, a unit cell equivalent to the simulation of the 2×2 unit cell has been used from which the aluminum slab has been removed. For the VASP calculations a cubic unit cell with a sidelength of 20 Å was used.

Method	HOMO / eV	LUMO / eV	GAP / eV
Gaussian 6-311G(d,p) ¹⁵⁻¹⁸ , OBC	-9,392	1,021	10,414
Gaussian 6-311++G(d,p) ¹⁵⁻¹⁸ , OBC	-9,413	-0,332	9,081
Gaussian cc-pVTZ ¹⁹⁻²⁴ , OBC	-9,404	0,810	10,214
Gaussian cc-pVQZ ¹⁹⁻²⁴ , OBC	-9,419	0,430	9,849
Gaussian cc-pV5Z ¹⁹⁻²⁴ , OBC	-9,424	0,160	9,583
Gaussian AUG-cc-pVTZ ¹⁹⁻²⁴ , OBC	-9,418	-0,376	9,042
FHI-aims, tight basis set (see section 2.1), OBC	-9,404	0,003	9,408
FHI-aims, tight basis set (see section 2.1), PBC	-9,436	-0,030	9,406
VASP, ENCUT = 700 eV, PBC	-9.383	-0.388	9.035
VASP, ENCUT = 1400 eV PBC	-9.417	-0.429	8.988

11. Electrical field for a CREST-type compensation charge

In the main manuscript it has been argued that the spurious collective electrostatic shifts of core-level binding energies in final-state calculations could be avoided by a CREST-like approach^{25,26} localizing the compensation charges statically in a charged sheet, rather than putting them into the lowest unoccupied states in the metal next to the Fermi level. In that case, the charged sheet would have to be placed above the adsorbate layer so that the field between the core holes and the compensation charges is primarily found above the adsorbate molecules and in this way cannot shift the positions of the core levels relative to the metal's Fermi level. A similar effect as with a charged sheet can also be achieved for point charges sufficiently far away from the interface (in the following plot at a distance of 30 Å).

As shown in Figure S20 for two differently sized unit cells, the field of that array of point charges (formed by the core holes and their compensation charges) decays rapidly on the substrate-side of the core holes (i.e. at negative distances), while it quickly approaches a constant value on the other side. This shows that in this way, spurious collective electrostatic shifts of core-level binding energies can indeed be avoided. What the plot, however, also shows is that the decay of the field on the substrate side is much faster than it would be for an isolated point charge. The field of the latter is, however, the field that triggers the screening effects in the metal, that are meant to be described by the final-state calculations. Consequently, a CREST-like compensation charge will result in an incorrect description of the core-hole screening, especially for small unit cells.

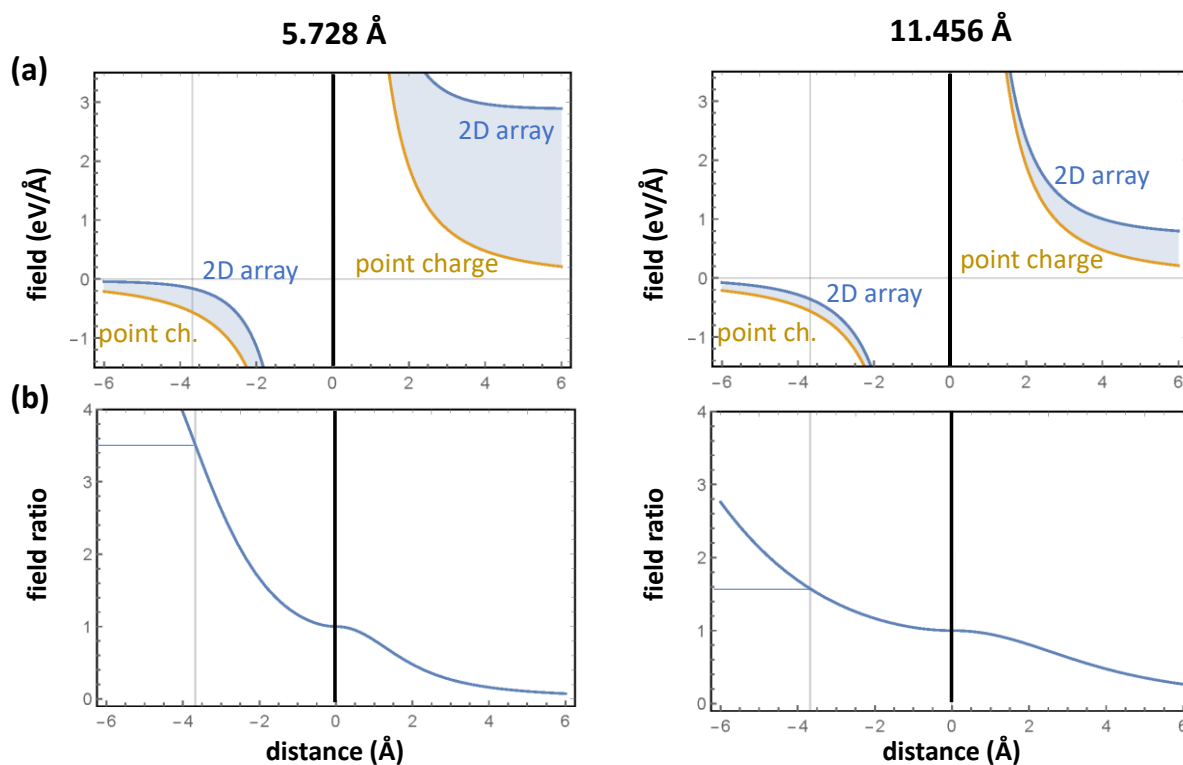


Figure S20. (a) Electric fields in z -direction generated by a point charge (light brown) and by two parallel 2D arrays of oppositely charged point charges (blue) as a function of the distance from one of the point charges. The absolute magnitude of each corresponds to the elementary charge (when considering half core-holes, the magnitudes of the fields need to be divided by two). The 2D point charge arrays are each arranged on a quadratic grid with a distance between the charges of 5.728 \AA (left panels, corresponding to the 2×2 unit cell) and 11.456 \AA (right panels, corresponding to the 4×4 supercell). The positively charged sheet is positioned at “distance” zero and represents periodically repeated core holes. The negative charges represent the compensation charges in a CREST-like approach and are positioned at a “distance” of $+30 \text{ \AA}$. The field is plotted along a line perpendicular to the planes of the arrays of charges. That line goes right through a pair of point charges. The thin line at -3.68 \AA relative to the core hole denotes the distance of the topmost aluminum layer from the core hole generated on the carbon atom of the methane. (b) Ratio of the two fields plotted in panel (a). The simulations have been performed using Mathematica²⁷.

12. References

- (1) Blum, V.; Gehrke, R.; Hanke, F.; Havu, P.; Havu, V.; Ren, X.; Reuter, K.; Scheffler, M. Ab Initio Molecular Simulations with Numeric Atom-Centered Orbitals. *Comput. Phys. Commun.* **2009**, *180* (11), 2175–2196. <https://doi.org/10.1016/j.cpc.2009.06.022>.
- (2) Hjorth Larsen, A.; Jørgen Mortensen, J.; Blomqvist, J.; Castelli, I. E.; Christensen, R.; Duřak, M.; Friis, J.; Groves, M. N.; Hammer, B.; Hargus, C.; Hermes, E. D.; Jennings, P. C.; Bjerre Jensen, P.; Kermode, J.; Kitchin, J. R.; Leonhard Kolsbjerg, E.; Kubal, J.; Kaasbjerg, K.; Lysgaard, S.; Bergmann Maronsson, J.; Maxson, T.; Olsen, T.; Pastewka, L.; Peterson, A.; Rostgaard, C.; Schiøtz, J.; Schütt, O.; Strange, M.; Thygesen, K. S.; Vegge, T.; Vilhelmsen, L.; Walter, M.; Zeng, Z.; Jacobsen, K. W. The Atomic Simulation Environment—a Python Library for Working with Atoms. *J. Phys. Condens. Matter* **2017**, *29* (27), 273002. <https://doi.org/10.1088/1361-648X/aa680e>.
- (3) Macdonald, J. R.; Barlow, C. A. Work Function Change on Monolayer Adsorption. *J. Chem. Phys.* **1963**, *39* (2), 412–422. <https://doi.org/10.1063/1.1734263>.
- (4) Maschhoff, B. L.; Cowin, J. P. Corrected Electrostatic Model for Dipoles Adsorbed on a Metal Surface. *J. Chem. Phys.* **1994**, *101* (9), 8138–8151. <https://doi.org/10.1063/1.468241>.
- (5) Monti, O. L. A. Understanding Interfacial Electronic Structure and Charge Transfer: An Electrostatic Perspective. *J. Phys. Chem. Lett.* **2012**, *3* (17), 2342–2351. <https://doi.org/10.1021/jz300850x>.
- (6) Natan, A.; Kuritz, N.; Kronik, L. Polarizability, Susceptibility, and Dielectric Constant of Nanometer-Scale Molecular Films: A Microscopic View. *Adv. Funct. Mater.* **2010**, *20* (13), 2077–2084. <https://doi.org/10.1002/adfm.200902162>.
- (7) De Renzi, V.; Rousseau, R.; Marchetto, D.; Biagi, R.; Scandolo, S.; del Pennino, U. Metal Work-Function Changes Induced by Organic Adsorbates: A Combined Experimental and Theoretical Study. *Phys. Rev. Lett.* **2005**, *95* (4). <https://doi.org/10.1103/PhysRevLett.95.046804>.
- (8) Zojer, E.; Taucher, T. C.; Hofmann, O. T. The Impact of Dipolar Layers on the Electronic Properties of Organic/Inorganic Hybrid Interfaces. *Adv. Mater. Interfaces* **2019**, *6* (14), 1900581. <https://doi.org/10.1002/admi.201900581>.
- (9) Slater, J. C. Atomic Shielding Constants. *Phys. Rev.* **1930**, *36* (1), 57–64. <https://doi.org/10.1103/PhysRev.36.57>.
- (10) Frisch, M. J.; Trucks, G. W.; Schlegel, H. B.; Scuseria, G. E.; Robb, M. A.; Cheeseman, J. R.; Scalmani, G.; Barone, V.; Petersson, G. A.; Nakatsuji, H.; Li, X.; Caricato, M.; Marenich, A. V.; Bloino, J.; Janesko, B. G.; Gomperts, R.; Mennucci, B.; Hratchian, H. P.; Ortiz, J. V.; Izmaylov, A. F.; Sonnenberg, J. L.; Williams-Young, D.; Ding, F.; Lipparini, F.; Egidi, F.; Goings, J.; Peng, B.; Petrone, A.; Henderson, T.; Ranasinghe, D.; Zakrzewski, V. G.; Gao, J.; Rega, N.; Zheng, G.; Liang, W.; Hada, M.; Ehara, M.; Toyota, K.; Fukuda, R.; Hasegawa, J.; Ishida, M.; Nakajima, T.; Honda, Y.; Kitao, O.; Nakai, H.; Vreven, T.; Throssell, K.; Montgomery, J. A., Jr.; Peralta, J. E.; Ogliaro, F.; Bearpark, M. J.; Heyd, J. J.; Brothers, E. N.; Kudin, K. N.; Staroverov, V. N.; Keith, T. A.; Kobayashi, R.; Normand, J.; Raghavachari, K.; Rendell, A. P.; Burant, J. C.; Iyengar, S. S.; Tomasi, J.; Cossi, M.; Millam, J. M.; Klene, M.; Adamo, C.; Cammi, R.; Ochterski, J. W.; Martin, R. L.; Morokuma, K.; Farkas, O.; Foresman, J. B.; Fox, D. J. *Gaussian 16 Revision A.03*; 2016.

- (11) Kresse, G.; Hafner, J. Ab Initio Molecular Dynamics for Liquid Metals. *Phys. Rev. B* **1993**, *47* (1), 558–561. <https://doi.org/10.1103/PhysRevB.47.558>.
- (12) Kresse, G.; Hafner, J. Ab Initio Molecular-Dynamics Simulation of the Liquid-Metal–Amorphous-Semiconductor Transition in Germanium. *Phys. Rev. B* **1994**, *49* (20), 14251–14269. <https://doi.org/10.1103/PhysRevB.49.14251>.
- (13) Kresse, G.; Furthmüller, J. Efficiency of Ab-Initio Total Energy Calculations for Metals and Semiconductors Using a Plane-Wave Basis Set. *Comput. Mater. Sci.* **1996**, *6* (1), 15–50. [https://doi.org/10.1016/0927-0256\(96\)00008-0](https://doi.org/10.1016/0927-0256(96)00008-0).
- (14) Kresse, G.; Furthmüller, J. Efficient Iterative Schemes for *Ab Initio* Total-Energy Calculations Using a Plane-Wave Basis Set. *Phys. Rev. B* **1996**, *54* (16), 11169–11186. <https://doi.org/10.1103/PhysRevB.54.11169>.
- (15) Petersson, G. A.; Bennett, A.; Tensfeldt, T. G.; Al-Laham, M. A.; Shirley, W. A.; Mantzaris, J. A Complete Basis Set Model Chemistry. I. The Total Energies of Closed-shell Atoms and Hydrides of the First-row Elements. *J. Chem. Phys.* **1988**, *89* (4), 2193–2218. <https://doi.org/10.1063/1.455064>.
- (16) Petersson, G. A.; Al-Laham, M. A. A Complete Basis Set Model Chemistry. II. Open-shell Systems and the Total Energies of the First-row Atoms. *J. Chem. Phys.* **1991**, *94* (9), 6081–6090. <https://doi.org/10.1063/1.460447>.
- (17) McLean, A. D.; Chandler, G. S. Contracted Gaussian Basis Sets for Molecular Calculations. I. Second Row Atoms, $Z = 11$ –18. *J. Chem. Phys.* **1980**, *72* (10), 5639–5648. <https://doi.org/10.1063/1.438980>.
- (18) Krishnan, R.; Binkley, J. S.; Seeger, R.; Pople, J. A. Self-consistent Molecular Orbital Methods. XX. A Basis Set for Correlated Wave Functions. *J. Chem. Phys.* **1980**, *72* (1), 650–654. <https://doi.org/10.1063/1.438955>.
- (19) Dunning, T. H. Gaussian Basis Sets for Use in Correlated Molecular Calculations. I. The Atoms Boron through Neon and Hydrogen. *J. Chem. Phys.* **1989**, *90* (2), 1007. <https://doi.org/10.1063/1.456153>.
- (20) Kendall, R. A.; Dunning, T. H.; Harrison, R. J. Electron Affinities of the First-Row Atoms Revisited. Systematic Basis Sets and Wave Functions. *J. Chem. Phys.* **1992**, *96* (9), 6796. <https://doi.org/10.1063/1.462569>.
- (21) Woon, D. E.; Dunning, T. H. Gaussian Basis Sets for Use in Correlated Molecular Calculations. III. The Atoms aluminum through Argon. *J. Chem. Phys.* **1993**, *98* (2), 1358. <https://doi.org/10.1063/1.464303>.
- (22) Peterson, K. A.; Woon, D. E.; Dunning, T. H. Benchmark Calculations with Correlated Molecular Wave Functions. IV. The Classical Barrier Height of the $H + H_2 \rightarrow H_2 + H$ Reaction. *J. Chem. Phys.* **1994**, *100* (10), 7410–7415. <https://doi.org/10.1063/1.466884>.
- (23) Wilson, A. K.; van Mourik, T.; Dunning, T. H. Gaussian Basis Sets for Use in Correlated Molecular Calculations. VI. Sextuple Zeta Correlation Consistent Basis Sets for Boron through Neon. *J. Mol. Struct. THEOCHEM* **1996**, *388*, 339–349. [https://doi.org/10.1016/S0166-1280\(96\)80048-0](https://doi.org/10.1016/S0166-1280(96)80048-0).
- (24) Davidson, E. R. Comment on “Comment on Dunning’s Correlation-Consistent Basis Sets.” *Chem. Phys. Lett.* **1996**, *260* (3–4), 514–518. [https://doi.org/10.1016/0009-2614\(96\)00917-7](https://doi.org/10.1016/0009-2614(96)00917-7).
- (25) Sinai, O.; Hofmann, O. T.; Rinke, P.; Scheffler, M.; Heimel, G.; Kronik, L. Multiscale Approach to the Electronic Structure of Doped Semiconductor Surfaces. *Phys. Rev. B* **2015**, *91* (7), 075311. <https://doi.org/10.1103/PhysRevB.91.075311>.

- (26) Erker, S.; Rinke, P.; Moll, N.; Hofmann, O. T. Doping Dependence of the Surface Phase Stability of Polar O-Terminated (000 $\bar{1}$) ZnO. *New J. Phys.* **2017**, *19* (8), 083012. <https://doi.org/10.1088/1367-2630/aa79e7>.
- (27) Wolfram Research, Inc. *Mathematica*; Version 11.3; Champaign, IL, 2018.